Chemical Research in Toxicology®

Subscriber access provided by UNIV OF WISCONSIN - MADISON

Article

Cobalt release from a nanoscale multiphase lithiated cobalt phosphate dominates interaction with Shewanella oneidensis MR-1 and Bacillus subtilis SB491

Peter L. Clement, Joshua E. Kuether, Jaya R. Borgatta, Joseph T. Buchman, Meghan S Cahill, Tian A Qiu, Robert J Hamers, Z. Vivian Feng, and Christy L. Haynes

Chem. Res. Toxicol., **Just Accepted Manuscript** • Publication Date (Web): 04 Feb 2020

Downloaded from pubs.acs.org on February 4, 2020

Just Accepted

"Just Accepted" manuscripts have been peer-reviewed and accepted for publication. They are posted online prior to technical editing, formatting for publication and author proofing. The American Chemical Society provides "Just Accepted" as a service to the research community to expedite the dissemination of scientific material as soon as possible after acceptance. "Just Accepted" manuscripts appear in full in PDF format accompanied by an HTML abstract. "Just Accepted" manuscripts have been fully peer reviewed, but should not be considered the official version of record. They are citable by the Digital Object Identifier (DOI®). "Just Accepted" is an optional service offered to authors. Therefore, the "Just Accepted" Web site may not include all articles that will be published in the journal. After a manuscript is technically edited and formatted, it will be removed from the "Just Accepted" Web site and published as an ASAP article. Note that technical editing may introduce minor changes to the manuscript text and/or graphics which could affect content, and all legal disclaimers and ethical guidelines that apply to the journal pertain. ACS cannot be held responsible for errors or consequences arising from the use of information contained in these "Just Accepted" manuscripts.

is published by the American Chemical Society. 1155 Sixteenth Street N.W., Washington, DC 20036

Published by American Chemical Society. Copyright © American Chemical Society. However, no copyright claim is made to original U.S. Government works, or works produced by employees of any Commonwealth realm Crown government in the course of their duties.

Title

Cobalt release from a nanoscale multiphase lithiated cobalt phosphate dominates interaction with *Shewanella oneidensis* MR-1 and *Bacillus subtilis* SB491

Authors

Peter L. Clement,[†] Joshua E. Kuether,[‡] Jaya R. Borgatta,[§] Joseph T. Buchman,[†] Meghan S. Cahill,[†] Tian A. Qiu, [†] Robert J. Hamers,[§] Z. Vivian Feng,[‡] Christy L. Haynes[*†]

Addresses

†University of Minnesota, Department of Chemistry, 207 Pleasant St. SE, Minneapolis, Minnesota 55455, United States
‡Augsburg University, Chemistry Department, 2211 Riverside Ave., Minneapolis, Minnesota 55454, United States
§Department of Chemistry, University of Wisconsin, 1101 University Avenue, Madison, Wisconsin 53706, United States

Abstract

Cobalt phosphate engineered nanomaterials (ENMs) are an important class of materials that find use in lithium ion battery cathodes, catalytic activity, and potential use in super capacitors. As production of these nanomaterials increases, so does the likelihood of their environmental release; however, to date, there are relatively few investigations of the impact of nanoscale metal phosphates on biological systems. Furthermore, nanomaterials used in commercial applications are often multiphase materials, and analysis of the toxic potential of mixtures of nanomaterials has been rare. In this work, we studied the interactions of two model environmental bacteria, *Shewanella oneidensis* MR-1 and *Bacillus subtilis* with a multiphase lithiated cobalt phosphate (mLCP) nanomaterial. Using a growth-based viability assay, we found that mLCP was toxic to both bacteria used in this study. To understand the observed toxicity, we screened for production of reactive oxygen species (ROS) and release of Co^{2+} from mLCP using three abiotic fluorophores. We also used Newport Green™ DCF dye to show that cobalt was taken up by the bacteria after

mLCP exposure. Using TEM, we noted that the mLCP was not associated with the bacterial cell surface. To further probe the mechanism of interaction of mLCP, the bacteria were exposed to an equivalent dose of cobalt ions that dissolved from mLCP, which recapitulated the changes in viability when the bacteria were exposed to mLCP, and it also recapitulated the observed bacterial uptake of cobalt. Taken together, this implicates the release of cobalt ions and their subsequent uptake by the bacteria as the major toxicity mechanism of mLCP. The properties of the ENM govern the release rate of cobalt, but the toxicity does not arise from nano-specific effects—and importantly the chemical composition of the ENM may dictate the oxidation state of the metal centers, and thus limits ROS production.

TOC image

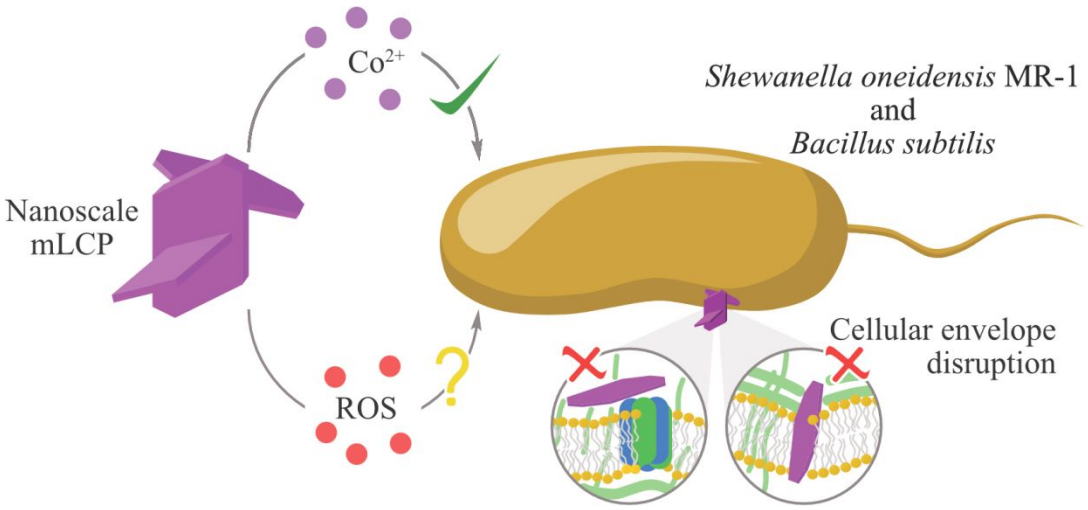
Co2+
Nanoscale
mLCP
ROS
?
Shewanella oneidensis MR-1
and
Bacillus subtilis
Cellular envelope
disruption

Introduction

Over the past 20 years, the prevalence of engineered nanomaterials (ENMs) in consumer products and industrial processes has dramatically risen.[1] In response, the field of nanotoxicology has rapidly developed to address concerns as the increased production, use, and disposal of ENM-containing products makes environmental release of ENMs more likely.[2, 3] A great deal of work in the field has shown that ENMs can exert deleterious effects towards organisms of varying complexity. Much of this work has focused on metal-based ENMs including: noble metals (*e.g.* Cu, Ag, Au),[4, 5] metal oxides (*e.g.* TiO_2, ZnO, SiO_2),[6, 7] and metal-containing quantum dots (*e.g.* CdSe, InP)[8, 9] because of the large-scale production of ENMs in these classes.[10] Furthermore, fruitful effort have developed an understanding of the chemical mechanisms by which metal-based ENMs may interact with bacteria, fungi, plants, cell lines, and animals.[11]

For metallic ENMs, some mechanisms of toxicity, such as perturbation of the cell wall, are dependent on the size and structure of an ENM and are often deemed "nano specific".[12, 13] Other mechanisms of toxicity include metal dissolution or reactive oxygen species (ROS) production, where the size and shape of an ENM may influence degree of release or production of toxic species,[11, 14] but the nanoparticles are not directly involved in toxic impacts.

Although these mechanisms have been extensively analyzed for nanoscale metal oxides and noble metals due to their commercial relevance,[15] mechanistic investigations of nanoscale metal phosphates have been rare. Nanoscale metal phosphates are a significant emerging class of ENMs because they show promise in agriculture,[16, 17] nutrition,[18] energy storage,[19-23] and catalysis.[24-27] For example, nanoscale $NH_4CoPO_4 \cdot H_2O$ has garnered interest as a supercapacitor anode, while $Li_{1-x}M_xPO_4$ (M = Fe, Ni, Mn, Co) nanomaterials have been investigated as next-generation lithium ion intercalation battery cathodes.[20-23] In the near future, nanoscale lithium

cobalt phosphate will find use in the cathodes of 5-V lithium ion batteries.[28, 29] Cobalt oxides with surface phosphate groups (e.g. the recently discovered so-called "Co-Pi" catalyst) and $Na_2CoP_2O_7$ are some of the most effective catalysts known for water oxidation.[24-27] Many applications of metal phosphates require materials in nanoparticle form; for example, $LiCoPO_4$ and the more common $LiFePO_4$, have high resistivity that limits their utility in energy storage applications as micron-sized particles, but this limitation can be alleviated by using nanoparticles <100 nm in size.[30-33] Similarly, catalytically active cobalt phosphate catalysts are used in nanostructured form to maintain high surface area and low electrical resistivity, both of which are important to obtain high catalytic efficiencies.[34]

One complication with metal phosphates, as with metal oxides, is the possibility of Co(II) and Co(III) metal centers, which has implications for ROS production. A differentiator between phosphate nanomaterials compared with oxide analogs is that phosphates have more complex crystal structures and frequently form mixtures of closely related hydroxy-phosphate structures.[35-37] Despite their structural complexity and the frequent presence of multiple phases, the widespread emergence of transition metal-based nanomaterials warrants the study of the potential environmental impacts of these materials. Yet, within the field of nanotoxicology, there has been little exploration of the interactions of nanoscale metal phosphates with organisms. Liu & Lal show that a $FePO_4$ dietary supplement reduces the metabolic activity of human colonic epithelial cells.[18] Melby et al. show that lithiated cobalt phosphate nanoparticles, synthesized in the same manner as the ENMs used in this work, induce minimal toxicity in trout gill epithelial cells when compared to a cobalt-containing metal oxide.[38, 39] Previous work by members of our group demonstrates that copper phosphate nanoparticles increase resistance of watermelon plants to deasese and increase fruit yields.[37] However, there is the unanswered question of whether nanoscale metal phosphates

generally follow the same rules of interactions understood for other classes of metal-based ENMs.[11]

In this work, we use a Gram-negative, metal-reducing bacterium *Shewanella oneidensis* MR-1, and a Gram-positive bacterium capable of nitrogen fixation, *Bacillus subtilis* SB491. We choose to work with environmental bacteria as they are low-trophic level organisms that may provide insights into broader environmental impacts in the case of unintentional release of nanoscale metal phosphates. While results using these two bacterial strains alone cannot be generalized to all bacteria, insights gained with these two model Gram-negative and Gram-positive bacterial strains point toward potential overarching interaction mechanisms. Our primary goals are to (a) determine if a nanoscale, multiphase lithiated cobalt phosphate negatively impacts the viability of both model bacteria, and (b) to study the contribution of (i) release of Co^{2+} ions, (ii) production of ROS, and (iii) cellular association of nanoparticles to any observed toxicity. Overall, we find that cobalt released through nanoparticle dissolution of nanoparticle is internalized in bacterial cells, and ultimately decreases viability of *S. oneidensis* MR-1 and *B. subtilis*.

Materials & Methods:

Reagents

We purchased *S. oneidensis* MR-1 BAA 1096 from ATCC and *B. subtilis* SB491 from the Bacillus Genetic Stock Center. In all experiments, we used ultrapure water (>18 MΩ·cm resistivity) from a Barnstead Nanopure system. We purchased 3′-aminophenyl fluorescein (APF), 2′,7′-dichlorofluorescin diacetate (H_2DCF-DA), and Newport Green™ 2′,7′-dichlorofluorescein diacetate (NPG DCF-DA) from Invitrogen (Thermo Fisher Scientific). We used a horseradish peroxidase (HRP) solution, which contained Triton-X and cholate, from Amplex™ Red Hydrogen

Peroxide/Peroxidase Assay Kit (Thermo Fisher Scientific). We list the remainder of the sources of the organic and inorganic reagents in the Supporting Information.

Material synthesis & characterization

Cobalt phosphate synthesis

We synthesized mLCP material as described elsewhere.[38] Briefly, we used a polyol method[40] with cobalt acetate tetrahydrate, diethylene glycol, ammonium phosphate dibasic, and lithium acetate dihydrate precursors. We washed the product with ethanol and dried it under reduced pressure overnight.

X-ray diffraction (XRD)

We deposited the nanomaterials onto a thin grease layer on a zero-diffraction plate (MTI Corporation, boron-doped silicon) and analyzed the sample using a Bruker Advanced Powder Diffractometer fitted with Cu-Kα source. Using DIFFRAC.EVA and CrystalDiffract software, we analyzed the diffraction patterns and identified phases present.

Scanning electron microscopy (SEM)

We prepared samples for SEM by sonication in a dilute ethanolic solution of nanomaterials in a bath sonicator for 5 minutes. We drop cast the solution onto a boron-doped silicon wafer and imaged the sample using a secondary electron detector on a LEO Supra55 VP scanning electron microscope.

Transmission electron microscopy (TEM)

We sonicated a 1 mg/mL suspension of mLCP in water for 10 minutes, then diluted the particles 10:1 into 190 proof ethanol, followed by an additional 30 second sonication. Immediately, we transferred 3 μL onto a 200-mesh carbon-stabilized Formvar TEM grid (Ted Pella, Inc.). We used a FEI Tecnai T12 transmission electron microscope at an operating voltage of 120 kV to

image the mLCP nanoparticles. We did not attempt to size particles because of the large polydispersity, but imaged several hundred particles to confirm the morphology observed in scanning electron microscopy.

Dynamic light scattering (DLS) & ζ-potential

We measured the hydrodynamic diameter and ζ-potential of mLCP nanoparticles in HEPES buffer (2 mM HEPES, 25 mM NaCl, pH 7.4) using a Brookhaven BIC ZetaPals with a 35 mW 660 nm laser and recorded four replicates of the ζ-potential using a Brookhaven ZetaPALS ζ-potential analyzer.

X-ray photoelectron spectroscopy (XPS)

To prepare samples for X-ray photoelectron spectroscopy, we pressed the mixed phase lithium cobalt phosphate like material in to indium foil on a copper substrate. The film was then analyzed using a Thermo Scientific K-alpha XPS (Waltham, MA) with an Al X-ray source. We performed peak fitting analysis using CasaXPS software.

Inductively-coupled plasma-optical emission spectroscopy (ICP-OES) & -mass spectrometry (ICP-MS)

We measured the release of Co from mLCP particles using inductively-coupled plasma optical emission spectroscopy (ICP-OES) and inductively-coupled plasma mass spectrometry (ICP-MS). For 5 concentrations of mLCP (100, 10, 1, 0.1, and 0 mg/L), we measured metal concentrations after one and two hours of suspension, equivalent to the start and end times used for biological assay exposures. To separate dissolved ions from particles, we centrifuged solutions at 17,000 × g for 10 minutes, transferred the supernatants into fresh HEPES buffer, and centrifuged at 200,000 × g for 30 minutes. We froze the supernatant from these samples to minimize evaporation prior to analysis by ICP-OES or ICP-MS. We acquired at least 3 analytical replicates

for each sample. We used a single-element cobalt standard stock solution at 1000 mg/L in 2% HNO_3 from Assurance SPEX CertiPrep.

Abiotic dye protocol

To screen for abiotic production or release of ROS and cobalt ions, we used three fluorescent probes: 3′-aminophenyl fluorescein (APF), 2′,7′-dichlorofluorescin diacetate (H_2DCF-DA), and Newport Green™ 2′,7′-dichlorofluorescein diacetate (NPG DCF-DA) with respective excitation and emission (ex./em.) wavelengths 493/522, 495/525, and 505/535 nm. We modified a methodology described elsewhere, in which APF and H_2DCF-DA were used to measure ROS production from pyrite particles.[41, 42] Prior to exposures, we diluted H_2DCF-DA and NPG DCF-DA (at 5 and 2 mM in anhydrous DMSO) 1:1 into 0.1 M NaOH for 30 minutes to deacetylate the dies. To prepare working solutions of the dyes, we diluted 5 mM APF in DMF, 2.5 mM base-treated H_2DCF-DA, or 1 mM base-treated NPG DCF-DA into HEPES buffer (at 50-, 100-, and 100-fold dilutions, respectively). We added 20 µL of dyes, along with combinations of 20 µL of 20 units/mL HRP, 100 µM H_2O_2, 1 mg/mL mLCP, and 1 mM $CoCl_2$, to give 200 µL total of the following exposures and controls: i. Negative Control; ii. Positive Control (HRP, H_2O_2); iii. Partial Positive Control 1 (H_2O_2); iv. Partial Positive Control 2 (HRP); v. Exposure (mLCP); vi. Partial Positive Control Interference Check (mLCP, HRP); vii. Positive Control Interference Check (HRP, H_2O_2, mLCP); and viii. Co^{2+} Control (100 µM $CoCl_2$). We report full data in the Table S1. We allowed exposures to incubate for 1 hour prior to reading absorbance at 600 nm and fluorescence at wavelengths noted above.

MINTEQ

We modeled equilibrium chemical speciation using Visual MINTEQ Version 3.1. To determine the oxidation state of dissolved cobalt, we entered components of the buffer ([HEPES]

= 2 mMolal, [NaCl] = 20 mMolal, pH = 7.4) and assumed 100 μMolal Co^{2+}, 100 μMolal Co^{3+}, or 50 μMolal Co^{2+} and 50 μMolal Co^{3+}. We then repeated this calculation with the Co^{2+}/Co^{3+} redox couple enabled. We analyzed both speciation and mass distribution to understand the predicted behavior of Co ion species under exposure conditions.

Biological characterization

We performed all incubations for *S. oneidensis* MR-1 and *B. subtilis* at 30 °C and 37 °C, respectively. We grew colonies of *S. oneidensis* MR-1 or *B. subtilis* on Luria-Bertani (LB) agar plates (1 L of H_2O, 25 g LB powder, 15 g agar) overnight and then transferred colonies into 10 mL of LB broth (1 L of H_2O, 25 g LB powder). We incubated this inoculant in an orbital shaker (300 RPM) for approximately 4 hours until bacteria reached the mid log phase, where optical density at 600 nm (OD_{600}) is between 0.3-0.6. We performed all exposures at room temperature using ENM or ion solutions made using HEPES buffer. Therefore, all negative controls comprised HEPES buffer added to cells for the exposure duration.

Preparation of bacteria for viability assays

We washed the bacteria in LB medium into HEPES buffer via single wash with Dulbecco's phosphate-buffered saline (DPBS) using a 10 minute, 750 × g centrifugation to pellet bacteria. The OD_{600} of the solution was adjusted to 0.1 using HEPES buffer, equivalent to 10^8 colony-forming units (CFU) per milliliter.

Colony counting viability assay

To validate viability results from the growth-based viability assay, we performed a colony counting assay for *S. oneidensis* MR-1. This was not performed on *B. subtilis* due to its swarming motility (a strain-specific behavior that makes it difficult to count colonies on traditional agar plates).[43] We exposed 20 μL NP suspensions (or HEPES buffer as negative control) to 180 μL of

the OD_{600} = 0.1 (10^8 CFU) stock suspension for 1 hour. We then serially diluted these exposed solutions to nominally 10^4 and 10^3 CFU/mL using dilution factors of 10. From each of these solutions, we dropped 10 µL onto LB agar plates (6 drops as technical replicates) that had been previously partially dried for 30-35 minutes and sterilized by UV illumination. We allowed bacteria to grow for 16-20 hours in a 30 °C incubator before counting the colonies. We normalized counts to the negative control within each plate.

Growth-based viability (GBV) assay

The experimental procedure and data processing for the growth-based viability (GBV) assay has been recently described elsewhere in detail.[44] Briefly, we consider the OD_{600} = 0.1 suspension of bacteria a negative control with 100% viability. A calibration curve was constructed for each bacterial strain by serially diluting the 100% viability stock. Nanoparticle exposures comprised 180 µL of the OD_{600} = 0.1 cells mixed with 20 µL of a 10× NP working solution. After a 1-hour exposure, we transferred 5 µL of exposed and calibration bacteria to 195 µL of LB broth in a 96-well plate. Using a BioTek Synergy 2 plate reader, we measured the OD_{600} of this 96-well plate overnight using 5 minute read-intervals at optimal growth temperatures for each bacteria strain. We processed data using RStudio, as previously explained,[44] and obtained estimates of cell viability by comparing the exposed bacteria to the linear calibration curve.

Newport Green™ 2′,7′-dichlorofluorescein assay for cobalt uptake

We washed bacteria inoculant by centrifugation (2000 × g, 5 minutes) into 30 mL of DPBS. To half of the stock, we added 30 µL of 2 mM NPG DCF-DA in DMSO (to give an incubation concentration of 4 µM). The second half of the bacteria stock served as a control for any auto-fluorescence and scattering from bacteria and ENMs. For dye loading, we incubated both tubes in a heated orbital shaker, at 30 and 37 °C for *S. oneidensis* and *B. subtilis*, respectively, for 45

minutes, followed by centrifugation at 3000 × g for 10 minutes and resuspension into HEPES buffer to remove extracellular dye. We exposed bacteria to mLCP or $CoCl_2$ in triplicate at 5 doses. We vortexed the exposed bacteria and incubated in the dark for 1 hour. We washed the bacteria twice, first into 1 mL HEPES buffer and then into 200 µL of HEPES buffer (10,000 × g, 5 minutes). Using a BioTek Synergy H1 Hybrid Reader, we measured the OD_{600} and fluorescence (ex./em. 505/535 nm) of these final solutions. In data analysis, we subtracted the average of the fluorescence signal from the undyed cells for each treatment condition and then calculated the turn-on ratio compared to the negative control of dyed cells by subtracting the average fluorescence of the negative control (F_0) from the average fluorescence of a given exposure condition (F) and then dividing by (F_0), i.e. $(F-F_0)/F_0$.

2′,7′-Dichlorofluorescin diacetate

The procedure for measurement of intracellular ROS by 2′,7′-dichlorofluorescin diacetate (H_2DCF-DA) is similar to that with NPG with minor changes. We incubated bacteria in 5 µM H_2DCF-DA dye in DMSO at 30 and 37 °C for *S. oneidensis* and *B. subtilis*, respectively, and measured fluorescence using excitation and emission at 493 and 522 nm, respectively. We used two different doses of H_2O_2 as positive controls for this assay (approximately 0.1 and 0.01% H_2O_2 in HEPES).

Brightfield and fluorescence optical microscopy

We placed NPG DCF-loaded bacteria on a microscope glass slide and, using a Leica AF6000 microscope, we obtained brightfield images. With a FITC filter (ex./em. maxima at 490/525 nm), we imaged the cells to discern whether the fluorescent signal from the NPG DCF was localized to cells identified in brightfield. We processed the images in ImageJ.

Resin-embedded TEM of biological samples

We prepared resin-embedded bacteria exposed to mLCP at 3 doses (100, 10, and 0 mg/L mLCP) using a previously described method given in detail in the Supporting Information.[45]

Statistical testing

Statistical analysis and curve fittings were performed using GraphPad Prism 6 software. We fit viability data with non-parametric curves using the four-parameter Hill equation. We constrained the maximum of the dose response curves to the average viability observed for negative controls. We carried out significance testing between groups throughout this work using 2-way analysis of variance (ANOVA) with Tukey's multiple comparison test. We performed outlier analysis using a one-sided Grubbs' test ($p < 0.05$). We note in the text where outliers are excluded and show the full data in the supporting information.

Results:

Synthesis of multiphase lithiated cobalt phosphate

We employ a polyol synthetic approach using cobalt acetate, ammonium phosphate, and lithium precursors with the goal of synthesizing nanoscale $LiCoPO_4$.[46] Previous studies have reported that synthesis of $LiCoPO_4$ frequently forms multiple chemical phases and structural polymorphs.[19, 37, 40, 47, 48] Similarly, analysis of the x-ray diffraction (XRD) trace for the synthesized material (Figure 1) shows that the product is a multiphase material with putative peak assignments to $[Co(H_2O)_6](H_2PO_2)_2$ (Crystallography Open Database (COD) code: 2012913), $NH_4[CoPO_4(H_2O)]$ (COD code: 2008122), and $LiC_2H_3O_2$ (COD code: 7206368). Based on the sharpness of peaks within the XRD trace, these phases appear to be crystalline. The XPS characterization, included in the supplementary information (Figure S1), shows Co peaks consistent with a 2+ oxidation state. ICP-OES data showed a relative composition of $Li_{0.2229\pm0.004}Co_1P_{0.8135\pm0.0006}$. Given the reported uses of $NH_4[CoPO_4(H_2O)]$ as both a supercapacitor

material and as a precursor of $LiCoPO_4$, we believe the multi-phased nature of the as-synthesized lithiated cobalt phosphate (mLCP) provides a good representation of the complexity in this class of materials.

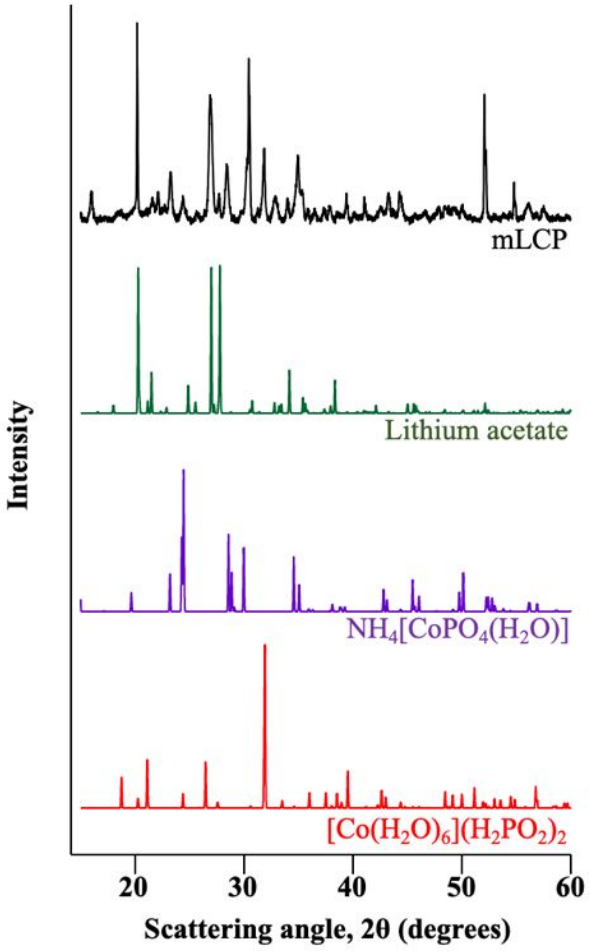

Figure 1. XRD trace of mLCP material (black) and three putatively assigned phases lithium acetate (green), $NH_4[CoPO_4(H_2O)]$ (purple), and $[Co(H_2O)_6(H_2PO_2)_2$ (red) in the synthesized material.

Both SEM and TEM (Figure 2) reveal a sheet-like morphology of the mLCP with a relatively broad distribution of dimensions for the large basal planes, ranging from 100 nm to several microns across. Instances of side-on views of the material reveal particle widths well below 100 nm. Dynamic light scattering (DLS) in HEPES buffer confirms the presence of particles with

high polydispersity (0.3 ± 0.1) and large size features (2200 ± 100 nm). Laser doppler electrophoresis measurements show a modestly negative electrophoretic mobility (-19 ± 5 mV).

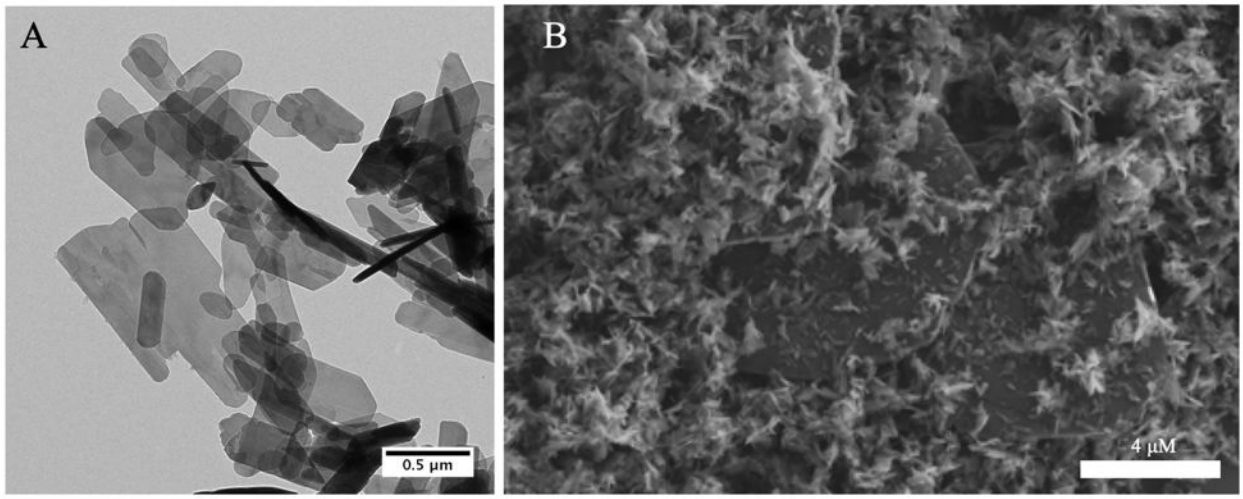

Figure 2. Representative TEM (A) and SEM (B) images of mLCP material.

Abiotic dye response

To assess potential routes of interaction between the synthesized nanoscale phosphate and the two bacteria used in this work, we use three fluorescent dyes to screen for chemical species generated by the nanomaterial. H_2DCF, APF, and NPG DCF each have turn-on fluorescence induced by general ROS (including singlet oxygen and peroxy radicals),[42] highly reactive oxygen species (hROS, including hydroxyl, peroxynitrite, perchlorite),[41] and certain divalent metals (Co^{2+}, Ni^{2+}, Zn^{2+}), respectively.[49, 50] Before use, we deacetylate H_2DCF-DA and NPG DCF-DA under alkaline conditions, removing groups that render the dyes cell permeant and block reactions to form fluorescent products. Response of each dye to conditions including cobalt ions and mLCP particles are shown in **Error! Reference source not found.** (full data of all conditions including positive controls can be found in Table S1). All three dyes show significant turn-on under oxidative conditions of H_2O_2 and horseradish peroxidase. The turn-on of NPG DCF under oxidative conditions is something to bear in mind when using this and metal binding dyes of the same class.

We find that the mLCP particles induce no APF turn-on fluorescence, but does induce fluorescence in NPG DCF, and a slight response for DCF. Although we cannot preclude the production of highly ROS from this ENM, any production is below our limit of detection. We can infer that the mLCP releases significant Co ion species into solution as response of NPG DCF to 100 mg/L mLCP is similar to that of 100 μM $CoCl_2$ (shown later as the high end of [Co^{2+}] released from the mLCP).

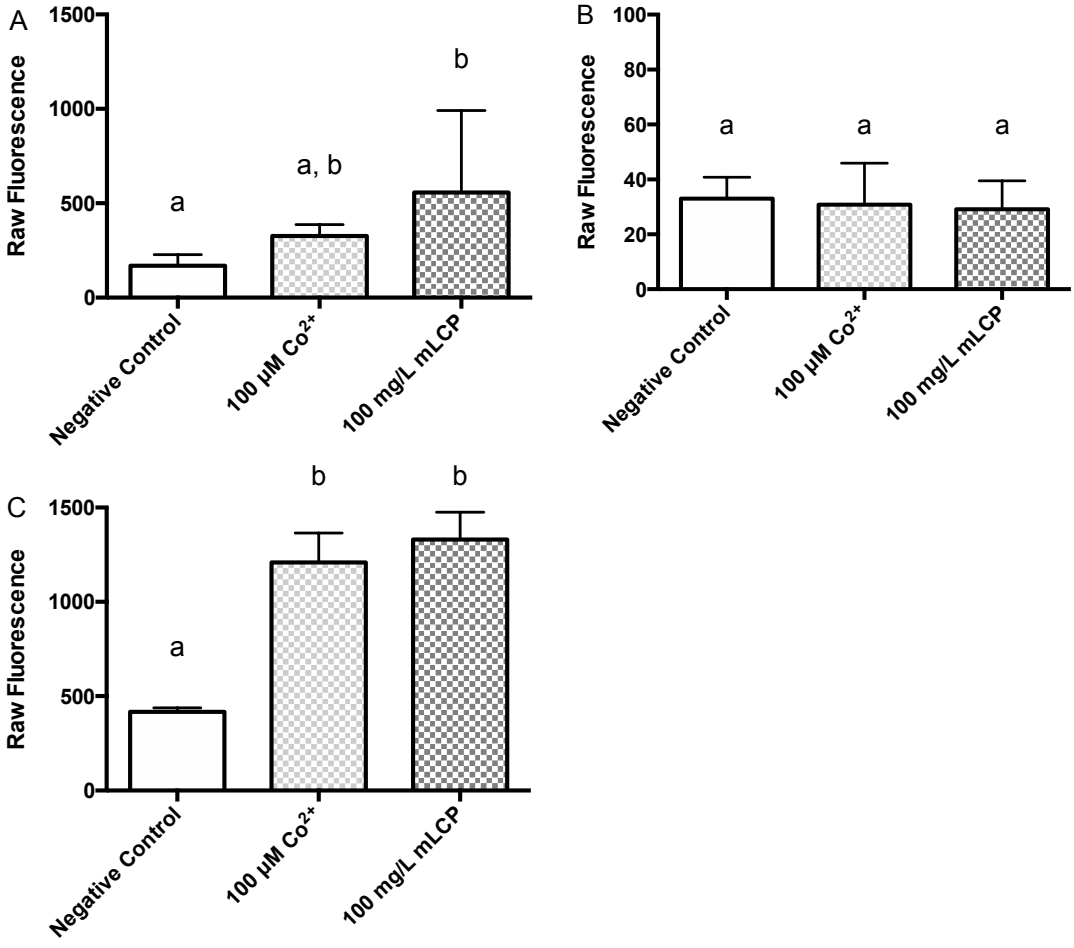

Figure 3. Abiotic fluorescence response of (a) H_2DCF, (b) APF, and (c) NPG DCF to mLCP and controls (ex./em. 505/535). Data for negative control, positive control (Co^{2+}), and mLCP responses represent material duplicates (of analytical triplicates). Data for positive control (HRP/H_2O_2) responses represent analytical triplicates. Error bars represent standard deviations, readings are grouped by statistical differences, $p < 0.05$, in a 2-way ANOVA.

To better quantify the release of Co species from the mLCP, we initially used ICP-OES. Due to the low concentrations of cobalt released from the mLCP, we analyzed further replicates by ICP-MS, which in our methods decreased sample processing time for low concentration samples. The ICP-OES replicate is well aligned with the ICP-MS replicates, and we thus include that data in Figure 4, which shows the Co release from the mLCP particles as determined. We performed these dissolution studies in the absence of bacteria at two time points based on the 1-hour bacterial exposure time, but we expect that the bacterial presence should not significantly change dissolution behavior, a phenomenon previously observed with lithium nickel manganese cobalt oxide materials.[reference to High Ni NMC] We remove all suspended mLCP particles using centrifugation and then ultracentrifugation. A lack of signal in dynamic light scattering confirms that this removal is effective. We find that both increasing the concentration of the mLCP and increasing the time that those particles incubate in HEPES buffer leads to increased release of Co species from the ENMs.

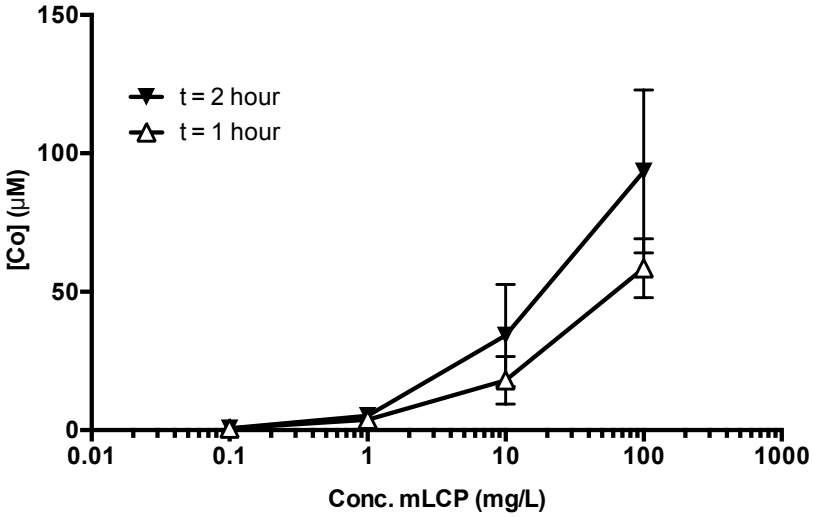

Figure 4. Cobalt release from mLCP in HEPES buffer as determined by ICP-OES and -MS. Time points represent the times at the beginning and end of bacterial exposures to mLCP. Data represents means of 4 replicates, with error bars representing standard deviation. Three replicates were recorded for 0.1 mg/L dissolution.

Using Visual MINTEQ 3.1, an equilibrium modeling software, we find that regardless of the initial oxidation state (+2 or +3) of the cobalt released, the majority of the cobalt species ends up as free Co^{2+} (aq), and virtually all of the cobalt species formally has cobalt in the 2+ oxidation state (Table S2). Past work has shown that if cobalt is initially present in materials in the 3+ oxidation state, its transformation to a solution-stable 2+ oxidation state may generate ROS.[51] However, in the identified phases of the synthesized material (shown in Figure 1) cobalt is formally in the 2+ oxidation state, eliminating this pathway for ROS generation. This in part explains why we do not observe oxidation of H_2DCF or APF (Figure 3).

Viability

Given the lack of ROS production observed by APF and DCF, our biological hypothesis was that the mLCP would negatively impact the viability of both *S. oneidensis* MR-1 and *B. subtilis* through release of toxic cobalt ions. We use a growth-based viability (GBV) assay (results from colony counting experiments for *S. oneidensis* can be seen in Figure S2) recently developed in our

groups[44] to measure the viability of both *S. oneidensis* MR-1 (Fig. **5a**) and *B. subtilis* (Fig. **5b**) to a range of nanoparticle doses (0, 0.1, 1, 10, 100 mg/L mLCP; see Figure S3 for particle mass-based dose-response curves). In parallel, we expose both bacteria to ions spanning the concentrations of dissolved species (0.01, 0.1, 1, 10, 100 μM $CoCl_2$). Four-parameter Hill plots allow for determination of IC_{50} values of 0.4 mg/L mLCP (0.3 to 0.5 mg/L, 95% confidence) and 2.5 μM $CoCl_2$ (1.9 to 3.4 μM, 95% confidence) for exposed S. *oneidensis* MR-1.

Figure 5 shows the response of the two bacteria to both mLCP and Co^{2+} plotted using the dose of soluble Co ions. For the $CoCl_2$ ions, this is simply the molar concentration of $CoCl_2$. For the mLCP exposures, we use the Co release at 1 hour as determined by ICP-OES as the effective dose. For *S. oneidensis* MR-1 (Figure 5a), we see a drastic decrease in viability as the dose of mLCP or $CoCl_2$ increases. There is very good agreement between the two curves, indicating that the release of cobalt from the mLCP may account for the toxicity.

For *B. subtilis* (Figure 5b), the GBV assay yields less reproducible results especially in response to $CoCl_2$ exposures. Upon removal of statistical outliers (full data presented in Figure S4 & S5), we see a similar decrease in viability for mLCP exposures as we find for *S. oneidensis* MR-1. Once again, the response to mLCP nanoparticles appears well within the error of the response to Co^{2+} ions; thus, it is plausible that Co^{2+} is the primary driver of toxicity. The IC_{50} values for *B. subtilis* we expose to mLCP and $CoCl_2$ are 0.1 mg/L mLCP (0.04 to 0.2 mg/L, 95% confidence) and 0.1 μM $CoCl_2$ (0.0003 to 40 μM, 95% confidence), respectively. The larger variability between biological replicates of *B. subtilis* exposed to $CoCl_2$ exposures leads to greater uncertainty in quantitative analysis of $CoCl_2$ toxicity to *B. subtilis*.

We find that the lowest-observed-adverse-effect level for *B. subtilis* is at 0.1 mg/L mLCP, while it was 1 mg/L for *S. oneidensis* MR-1, indicating a potentially higher susceptibility of *B.*

subtilis to Co^{2+} exposures. This finding is in line with our knowledge of response of these two bacteria to cobalt-containing metal oxides as well as other nanomaterials,[45] and improved metal handling by *S. oneidensis* MR-1 may have evolved alongside its ability to engage in redox cycles with a number of transition metals.

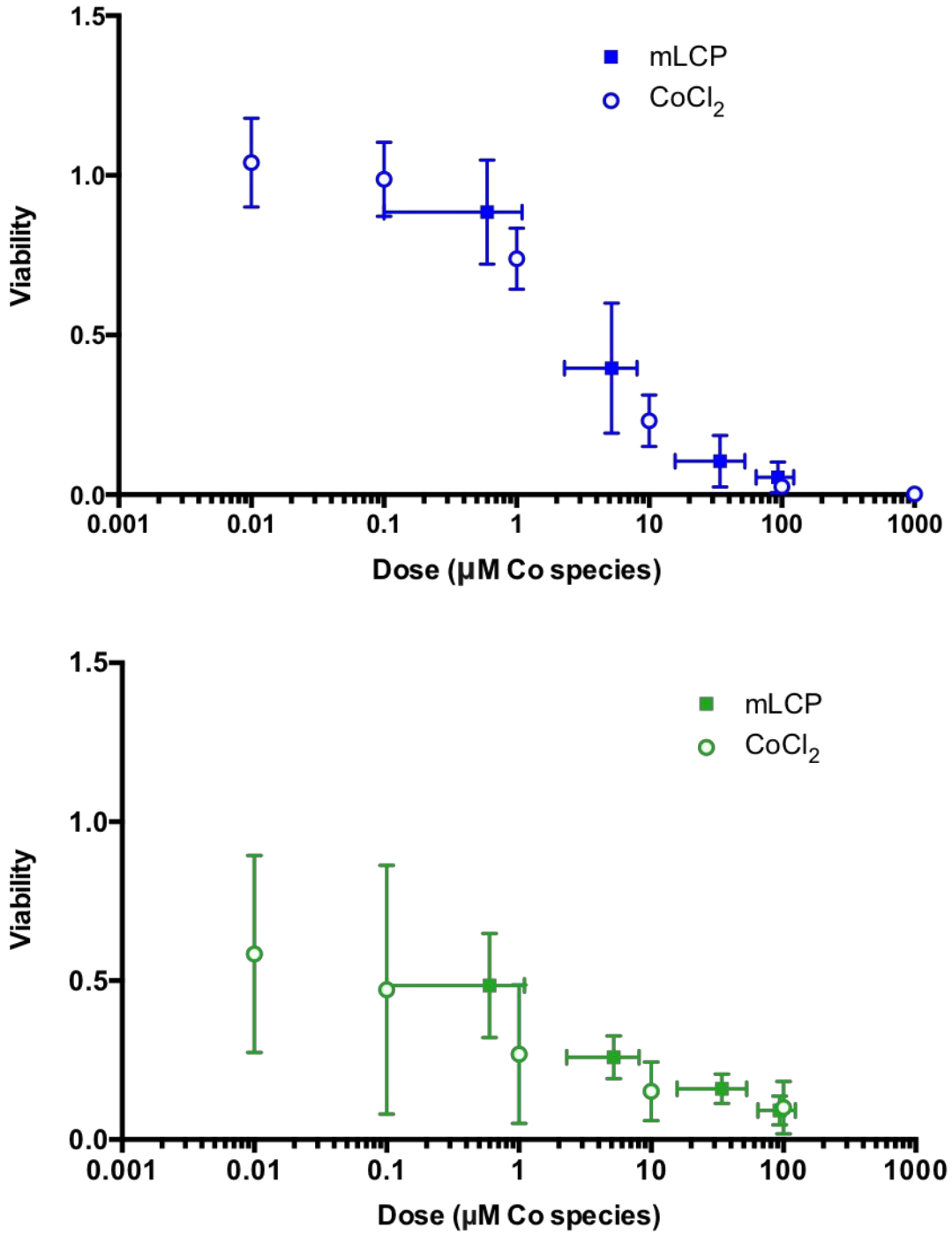

Figure 5. Viability of *S. oneidensis* MR-1 (top) and *B. subtilis* (bottom) exposed to either mLCP (solid squares) or $CoCl_2$ (open circles), as determined by GBV. Doses are presented based on soluble [Co^{2+}] at 2 hours of particles in HEPES, as determined by ICP-OES and -MS for mLCP. Data for *S. oneidensis* MR-1 represent means of biological triplicates; data for *B. subtilis* represent means of four biological replicates. Error bars represent standard deviations.

Newport Green™ DCF Assay

To further understand the role that cobalt plays in toxicity, we look for evidence of internalization of Co^{2+} into the bacteria. We use the NPG DCF-DA dye to achieve this. The dye is an acetylated fluorescein derivative with a di-(2-picolyl)amine metal binding domain, which has turn-on fluorescence once it is internalized into cells, deacetylated by intracellular esterases, and binds specific divalent metals (Zn^{2+}, Ni^{2+}, Co^{2+}). We optimize dye loading conditions to enhance signal from intracellular fluorescence versus extracellular background fluorescence. In Figures S6 and S7, we show that for *S. oneidensis* MR-1 and *B. subtilis* loaded with NPG DCF exposure to $CoCl_2$ leads to a slight increase in background fluorescence and a much higher fluorescence localized to distinct bacteria (which we identify in bright field imaging).

After loading bacteria with dye, we treated them with either mLCP (0, 0.1, 1, 10, 100 mg/L) or $CoCl_2$ (0, 0.1, 1, 10, 100 μM) for one hour. Figure 6a and Figure 6b show the fluorescent response of *S. oneidensis* MR-1 and *B. subtilis*, respectively. Here, we once again used exposure doses based on the concentration of cobalt species released (plots by mass dose shown in Figure S3). For both bacteria, increasing the dose of Co species, whether delivered by mLCP or $CoCl_2$, yields a dose-dependent increase in intracellular fluorescence. For *S. oneidensis* MR-1 (Figure 6a), we see very good agreement between the fluorescent signal arising from mLCP and $CoCl_2$ exposure, which indicates that the mLCP is not disrupting cellular structure or function in a way that significantly increases the susceptibility of the bacteria to uptake Co^{2+} ions.

For *B. subtilis,* we see similar trends in fluorescence for the bacteria when treated with Co^{2+} or mLCP. The fluorescence response of NPG DCF-loaded *B. subtilis* begins to increase at the 1 μM dose of $CoCl_2$, whereas for *S. oneidensis* MR-1 the uptake is observed at 10 μM $CoCl_2$. This could help us understand the increased susceptibility in terms of viability for *B. subtilis* to both mLCP and Co^{2+}.

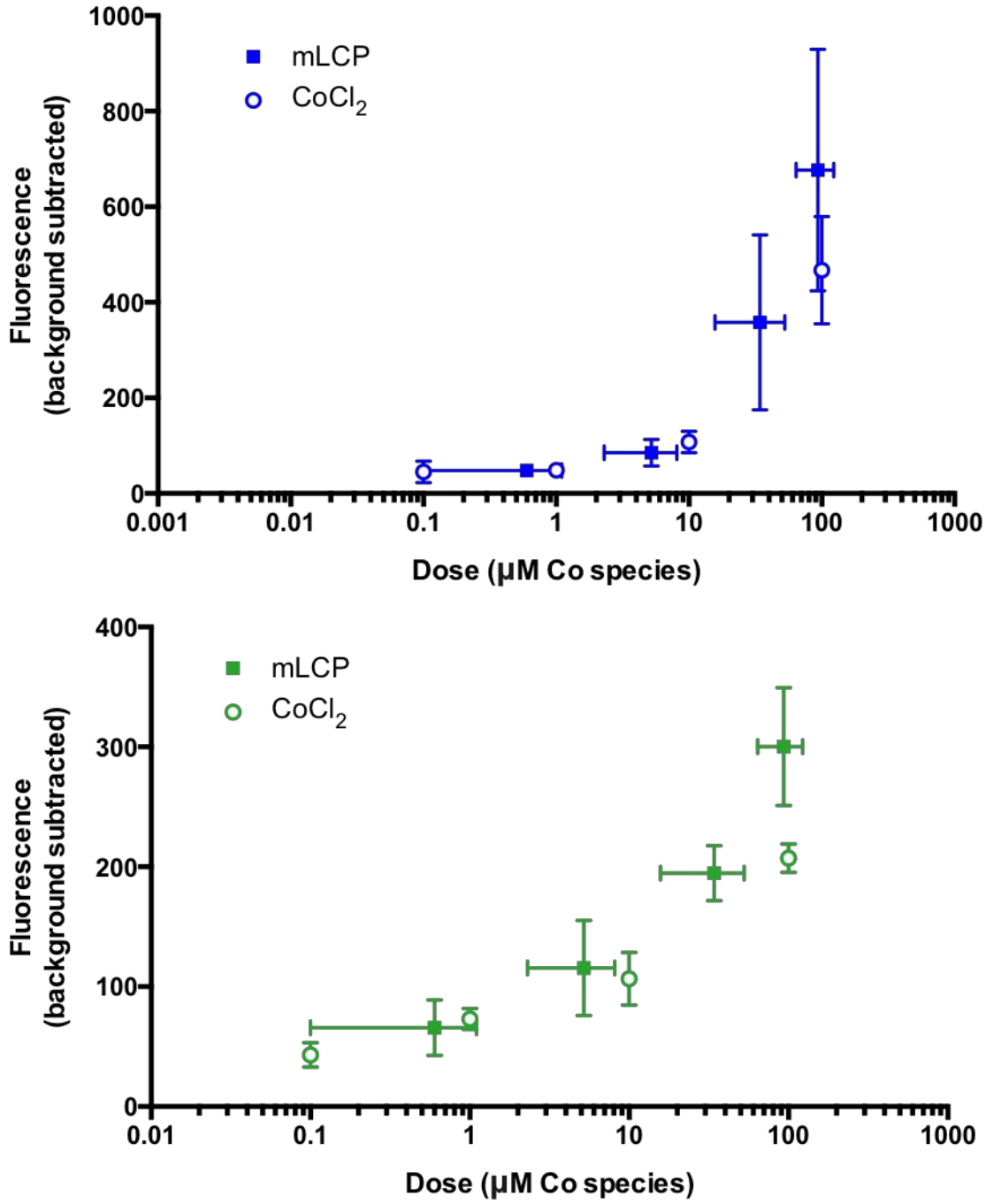

Figure 6. Fluorescence response of *S. oneidensis* MR-1 (A) and *B. subtilis* (B) loaded with Newport Green™ DCF dye that were exposed to either mLCP or $CoCl_2$ (ex./em. 505/535). Doses are presented based on soluble [Co] at 2 hours of particles in HEPES, as determined by ICP-OES and -MS for mLCP. Data for *S. oneidensis* MR-1 and *B. subtilis* represent means of biological triplicates, and error bars represent standard deviations.

2′,7′-Dichlorofluorescin assay

We are also interested in assessing the extent that nanoscale mLCP induces increases in intracellular levels of ROS. Intracellular ROS may originate from low-level production of ROS directly from the mLCP nanoparticles or by downstream effects of cobalt internalization and cell dysregulation. To measure intracellular ROS, we use the H_2DCF-DA dye. Despite literature precedent of using H_2DCF-DA to study bacteria, this dye is inconsistent in our hands with positive controls of H_2O_2 at times yielding no measurable intracellular fluorescence. The data we present is only from trials in which a positive control provides a statistically significant signal. We find (Figure 7) that the highest dose of mLCP causes a significant increase in H_2DCF-DA fluorescence, indicating an intracellular increase in ROS. The change is approximately 2-fold, so the biological significance of this change is unclear, but likely low. For *S. oneidensis* MR-1, we do not detect intracellular ROS when treated with the two highest doses of mLCP. We cannot rule out increases in intracellular ROS for the bacterium, but instead can say that the response is below the response that of 3 mM H_2O_2 induces.

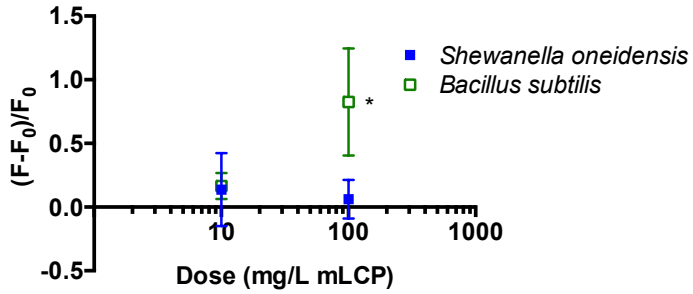

Figure 7. H2DCF-DA assay fluorescence response of *S. oneidensis* MR-1 and *B. subtilis* to mLCP exposures. Data for *S. oneidensis* MR-1 represent means of biological triplicates. Data for *B. subtilis* represent means of triplicates from a single day. Error bars represent standard deviations (* represents $p < 0.05$ relative to negative control.)

Biological TEM

It is clear that cobalt ions are taken up inside the bacteria, thus it is important to characterize whether or not the mLCP particles localize on or near the bacterial cells. Resin-embedded TEM is

an ideal way to determine if nanomaterials are either taken up into organisms[52] or assembled onto bacterial cell surfaces.[45] Upon examination of resin-embedded *S. oneidensis* MR-1 and *B. subtilis* exposed to mLCP at doses of 0 and 100 mg/L mLCP, we find no evidence of association between bacteria and the nanomaterial. In fact, we do not observe the presence of mLCP in the resin slices at even the highest doses. The colloidal instability of the material in aqueous suspensions leads to rapid settling, which may decrease likelihood of direct interaction of the nanomaterial with bacteria. In both energy storage and catalysis applications, metal phosphates will be used in the solid state, and so to better represent how this material is made and used on large scales we made no attempt to increase the colloidal stability in these experiments.

At high doses of mLCP exposure to *S. oneidensis*, we observe instances of separation of the cell wall from the cytoplasm, indicating cell lysis (red arrows in Figure 8c indicate examples of lysed cells). This phenomenon has been observed before with TEM images of lysed cells.[53] However, it is important to note that a fixed cell slice used for TEM analysis only shows the morphological consequence of lysis, but no dynamic information. For *B. subtilis*, exposure of mLCP induces no clear morphological changes. While TEM images such as these can give some qualitative insight into cell morphology, it is important to note the limitations of a technique that has an inherently low sample size and represents a single time point within a dynamic system.

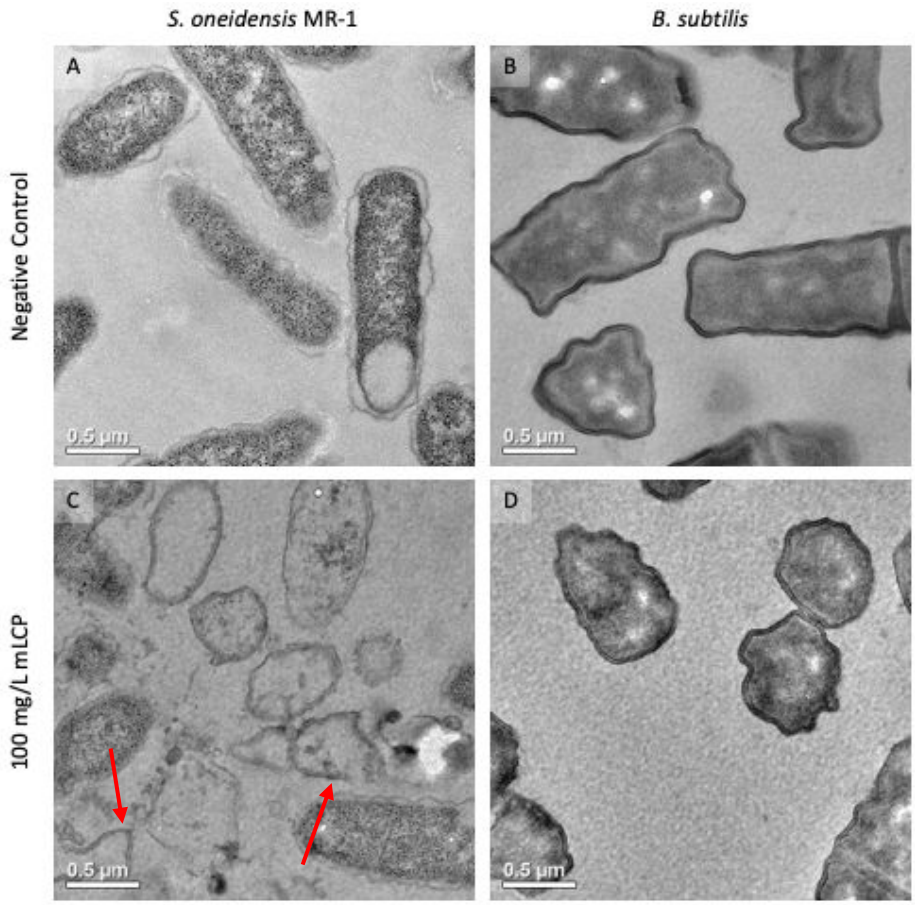

Figure 8. Representative resin-embedded TEM images of *S. oneidensis* MR-1 and *B. subtilis* exposed to 0 mg/L mLCP (A, B) or 100 mg/L mLCP (C, D) in HEPES buffer. Red arrows point to two instances of cell lysis, indicated by a fractured cell wall that does not contain cytoplasm.

Discussion

In this work, we describe the synthesis and characterization of a mLCP nanomaterial, which decreases the viability of two environmental model bacteria. We identify several potential routes of toxicity for a multiphase material, which we depict in Figure 9. We use three fluorophores with reactivity-based turn-on fluorescence to screen for production of ROS and heavy metal release. While we see no evidence for production of ROS, we qualitatively observe release of Co^{2+}, which we then quantify using ICP techniques. We do not find association of the ENM with the cell wall by resin-embedded TEM but observe cell wall damage for mLCP-exposed *S. oneidensis* MR-1. The H_2DCF-DA dye shows no intracellular increases of ROS within *S. oneidensis* MR-1

and a modest, and likely biologically insignificant, increase in *B. subtilis* upon exposure to mLCP. Notably, the NPG DCF-DA dye detects Co^{2+} internalization after dosing with mLCP, at levels which are recapitulated by doses of Co^{2+} equivalent to the species released from the mLCP for both *S. oneidensis* and *B. subtilis*. The use of cell-permeant probes to interrogate the cellular state beyond a viable vs. non-viable dichotomy helps close the knowledge gap between release of ions from nanomaterials and decreases in viability. These findings, along with the good agreement between dose-response curves based on dosing of soluble cobalt species indicates that for this multiphase cobalt phosphate, Co^{2+} ions are the primary driver of toxicity for both bacteria investigated in this study.

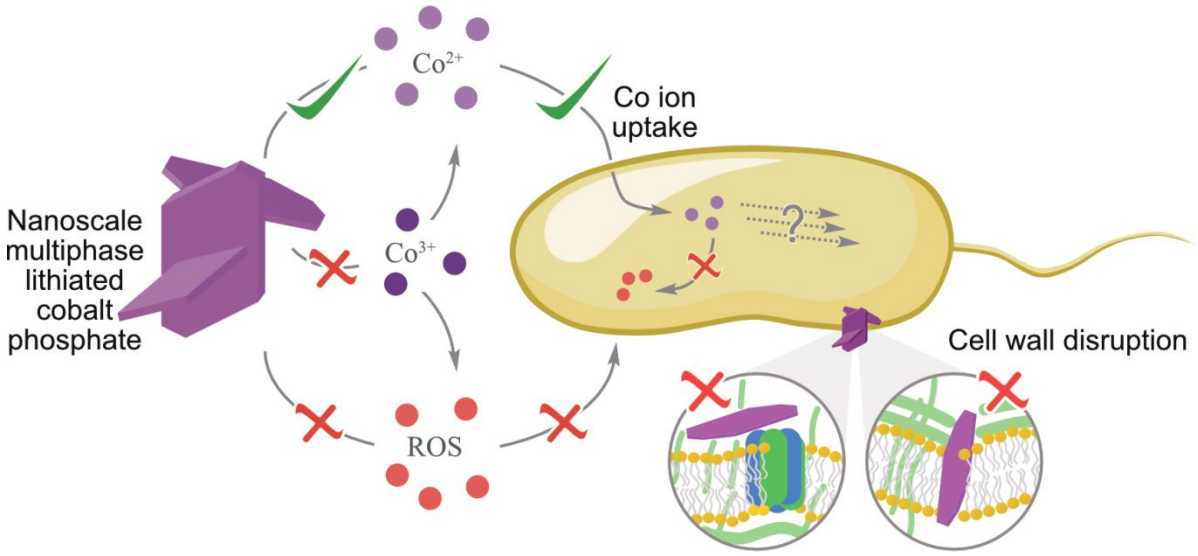

Figure 9. Summary of likely interactions between nanoscale mLCP and bacteria, as determined in this work.

Previous studies of dissolved heavy metals with bacteria shed light on the mechanism of the toxicity we observe. Transition metal ions are known to interact with cell walls,[54, 55] in particular when released from nanomaterials,[56] or to be internalized via high-affinity import systems.[57, 58] In bacteria, it has been shown that internalization of Co^{2+} leads to toxicity through disruption of the formation of iron-sulfur enzymes[59] and potential downstream interactions with DNA. It is debated in the literature whether increased Co^{2+} levels yield increases in intracellular

ROS in bacteria, with some reports showing Co^{2+} yielding increased fluorescence response of H_2DCF,[44] while others find no evidence of upregulation of ROS defense pathways.[45] However, it should be noted that H_2DCF is a less precise read-out of oxidative stress than other methods such as analysis of tail length in comet assays or changes in gene expression.[46]

The decreased viability we observe for the two bacteria are in line with those in literature reports on Co^{2+} toxicity towards bacteria. Ranquet et al. finds that in glucose-containing M9 medium, 100 μM $CoCl_2$—which is the highest dose in this work—significantly delays the growth of *Escherichia coli*, and that agar plates containing 700 μM $CoCl_2$ are bactericidal toward wild-type *E. coli*.[59] Also, in work by Thorgersen and Downs, 160 μM $CoCl_2$ in glucose-containing minimal medium significantly delays the onset of exponential growth of *Salmonella enterica*.[60] In both works, inclusion of iron ions successfully mitigates toxicity.[59, 60] Elevated levels of ferrous ions are able to outcompete cobaltous ions and maintain proper Fe-S cluster synthesis.[61] Given that cobalt phosphates are of interest for energy storage, and that iron phosphates are also used in energy storage applications, one potential route to mitigate toxicity of these materials may be synthesizing materials using combinations of Fe and Co.

This work develops knowledge surrounding two emerging questions in the field of nanotoxicology: 1) how do we assess the toxicity of materials that are inherently heterogeneous? and 2) can we transfer the rules developed for understanding metal oxide ENM toxicity to metal phosphate ENM toxicity?

While many nanoparticles are used in applications as single-phase materials, it is now recognized that surface chemical and physical transformations occur that can add additional complexity to materials. A clear challenge in the field of toxicology, and in particular nanotoxicology, is building a mechanistic understanding of how multiphase and heterogeneous

materials interact with organisms. The multiphase nature of the ENM we synthesize and study in this work precludes knowing the exact chemical composition of the material. This makes it difficult to predict material properties such as dissolution, electroactivity, or likelihood of association with organisms. However, via materials characterization we can to generate hypotheses about likely routes of interactions with bacteria, and then screen the nanomaterial production of toxicants using three fluorescent dyes. In doing so, we can understand the relevant behavior of the material without much more involved characterization. This approach is readily adaptable as numerous commercial fluorophores are on the market for various chemical of species.

Another open question this work addresses is whether biological systems interact with metal phosphates by fundamentally different mechanisms than they do with metal oxide ENMs. This question is an important one given the high likelihood of increased production, use, and disposal of nanoscale metal phosphates, and the dearth of research looking at the impact of metal phosphate ENMs on organisms, and specifically bacteria. Past works show that release of transition metal ions from metal oxide ENMs can play a major role in interactions with organisms.[11,37,47] This is in line with the mechanism of interaction between the mLCP and the two bacteria in this work. In other cases, ROS generation drives metal oxide toxicity. One well-documented mechanism of ROS generation for ENMs is production at electroactive surfaces. Although the mLCP contains potential energy storage and catalysis materials, we find little evidence of ROS generated from the ENM. A less studied mechanism of ROS generation is the process of redox-mediated dissolution.[14, 51] Some cobalt-containing oxides (e.g. $CoFe_2O_4$) contain Co(II), others (e.g. Co_3O_4) contain both Co(II) and Co(III), and materials of interest in energy storage (e.g. $LiCoO_2$, $LiNi_{0.33}Mn_{0.33}Co_{0.33}O_2$) often contain Co(III) centers. Yet dissolved Co^{3+} is not stable at physiological pH, and thus as Co(III) dissolves it will undergo reduction to Co^{2+}, with

the potential generation of ROS. Examination of the XRD-identified phases for mLCP shows that cobalt is formally present only as Co(II), meaning ROS generation through redox-mediated dissolution is not a significant pathway. Clearly metal oxidation state is an important factor in the toxic potential of a material, and it is a potential differentiator between some transition metal phosphates and oxides.

This work shows that for nanoscale metal phosphates the release of transition metals may serve as the primary interaction of ENMs with organisms, which is also the case for some metal oxides but not others where ROS interactions dominate. The relative importance of ROS generation, surface association, and uptake will undoubtedly vary for different materials and different organisms. Whether, in general, rules developed to understand metal oxide toxicity towards organisms hold for nanoscale metal phosphates requires more studies like those presented herein. And as nanomaterials continue to increase in complexity it is important to develop tools, like those we use here, that enable us to investigate the toxic potential of materials.

Acknowledgements

This work was supported by the National Science Foundation under the Center for Sustainable Nanotechnology CHE-1503408. The Center for Sustainable Nanotechnology is part of the Centers for Chemical Innovation Program. J.T.B. gratefully acknowledges support from a National Science Foundation GRFP (Grant #00039202). We thank Fang Zhou for microtome sectioning of the resin-embedded bacteria samples for TEM analysis. Transmission electron microscopy imaging was carried out in the Characterization Facility, University of Minnesota, which receives partial support from the NSF through the MRSEC program. We thank Elizabeth Lundstrom for performing ICP-OES and ICP-MS analysis as part of the University of Minnesota

Earth Sciences department. We thank Thomas Pho of Augsburg University for fluorescence and brightfield microscopy of NPG DCF-loaded bacteria.

Author Information

Corresponding Author *E-mail: chaynes@umn.edu.

Supporting Information. Reagents, abiotic fluorescence assay results, equilibrium simulations, XPS characterization of nanomaterials, ion control bacterial toxicity results, imaging of ions in bacteria, TEM sample preparation procedure.

References

(1) Lohse, S. E., and Murphy, C. J. (2012) Applications of Colloidal Inorganic Nanoparticles: From Medicine to Energy. *Journal of the American Chemical Society 134*, 15607-15620.

(2) Nel, A., Xia, T., Mädler, L., and Li, N. (2006) Toxic potential of materials at the nanolevel. *Science 311*, 622-627.

(3) Oberdörster, G., Oberdörster, E., and Oberdörster, J. (2005) Nanotoxicology: An Emerging Discipline Evolving from Studies of Ultrafine Particles. *Environmental Health Perspectives 113*, 823-839.

(4) Lin, J., Zhang, H., Chen, Z., and Zheng, Y. (2010) Penetration of Lipid Membranes by Gold Nanoparticles: Insights into Cellular Uptake, Cytotoxicity, and Their Relationship. *ACS Nano 4*, 5421-5429.

(5) Maurer, L. L., and Meyer, J. N. (2016) A systematic review of evidence for silver nanoparticle-induced mitochondrial toxicity. *Environ. Sci.: Nano 3*, 311-322.

(6) Maurer-Jones, M. A., Christenson, J. R., and Haynes, C. L. (2012) TiO2 nanoparticle-induced ROS correlates with modulated immune cell function. *Journal of Nanoparticle Research 14*.

(7) Tong, T., Wilke, C. M., Wu, J., Binh, C. T. T., Kelly, J. J., Gaillard, J.-F., and Gray, K. A. (2015) Combined Toxicity of Nano-ZnO and Nano-TiO 2 : From Single- to Multinanomaterial Systems. *Environmental Science & Technology 49*, 8113-8123.

(8) Khalili Fard, J., Jafari, S., and Eghbal, M. A. (2015) A Review of Molecular Mechanisms Involved in Toxicity of Nanoparticles. *Advanced Pharmaceutical Bulletin 5*, 447-454.

(9) Xu, G., Lin, G., Lin, S., Wu, N., Deng, Y., Feng, G., Chen, Q., Qu, J., Chen, D., Chen, S., Niu, H., Mei, S., Yong, K.-T., and Wang, X. (2016) The Reproductive Toxicity of CdSe/ZnS Quantum Dots on the in vivo Ovarian Function and in vitro Fertilization. *Scientific Reports 6*.

(10) Piccinno, F., Gottschalk, F., Seeger, S., and Nowack, B. (2012) Industrial production quantities and uses of ten engineered nanomaterials in Europe and the world. *Journal of Nanoparticle Research 14*.
(11) Zhang, H., Ji, Z., Xia, T., Meng, H., Low-Kam, C., Liu, R., Pokhrel, S., Lin, S., Wang, X., Liao, Y.-P., Wang, M., Li, L., Rallo, R., Damoiseaux, R., Telesca, D., Mädler, L., Cohen, Y., Zink, J. I., and Nel, A. E. (2012) Use of Metal Oxide Nanoparticle Band Gap To Develop a Predictive Paradigm for Oxidative Stress and Acute Pulmonary Inflammation. *ACS Nano 6*, 4349-4368.
(12) Kong, B., Seog, J. H., Graham, L. M., and Lee, S. B. (2011) Experimental considerations on the cytotoxicity of nanoparticles. *Nanomedicine 6*, 929-941.
(13) Xia, T., Kovochich, M., Liong, M., Zink, J. I., and Nel, A. E. (2008) Cationic Polystyrene Nanosphere Toxicity Depends on Cell-Specific Endocytic and Mitochondrial Injury Pathways. *ACS Nano 2*, 85-96.
(14) Hang, M. N., Hudson-Smith, N. V., Clement, P. L., Zhang, Y., Wang, C., Haynes, C. L., and Hamers, R. J. (2018) Influence of Nanoparticle Morphology on Ion Release and Biological Impact of Nickel Manganese Cobalt Oxide (NMC) Complex Oxide Nanomaterials. *ACS Applied Nano Materials 1*, 1721-1730.
(15) Keller, A. A., and Lazareva, A. (2014) Predicted Releases of Engineered Nanomaterials: From Global to Regional to Local. *Environmental Science & Technology Letters 1*, 65-70.
(16) Giroto, A. S., Guimarães, G. G. F., Foschini, M., and Ribeiro, C. (2017) Role of Slow-Release Nanocomposite Fertilizers on Nitrogen and Phosphate Availability in Soil. *Scientific Reports 7*.
(17) Liu, R., and Lal, R. (2015) Synthetic apatite nanoparticles as a phosphorus fertilizer for soybean (Glycine max). *Scientific Reports 4*.
(18) von Moos, L. M., Schneider, M., Hilty, F. M., Hilbe, M., Arnold, M., Ziegler, N., Mato, D. S., Winkler, H., Tarik, M., Ludwig, C., Naegeli, H., Langhans, W., Zimmermann, M. B., Sturla, S. J., and Trantakis, I. A. (2017) Iron phosphate nanoparticles for food fortification: Biological effects in rats and human cell lines. *Nanotoxicology 11*, 496-506.
(19) Amine, K., Yasuda, H., and Yamachi, M. (2000) Olivine LiCoPO4 as 4.8 V Electrode Material for Lithium Batteries. *Electrochemical and Solid-State Letters 3*, 178-179.
(20) Aravindan, V., Gnanaraj, J., Lee, Y.-S., and Madhavi, S. (2013) LiMnPO4 – A next generation cathode material for lithium-ion batteries. *Journal of Materials Chemistry A 1*, 3518-3539.
(21) Hu, M., Pang, X., and Zhou, Z. (2013) Recent progress in high-voltage lithium ion batteries. *Journal of Power Sources 237*, 229-242.
(22) Padhi, A. K., Nanjundaswamy, K. S., and Goodenough, J. B. (1997) Phospho-olivines as Positive-Electrode Materials for Rechargeable Lithium Batteries. *Journal of The Electrochemical Society 144*, 1188-1194.
(23) Rui, X., Zhao, X., Lu, Z., Tan, H., Sim, D., Hng, H. H., Yazami, R., Lim, T. M., and Yan, Q. (2013) Olivine-Type Nanosheets for Lithium Ion Battery Cathodes. *ACS Nano 7*, 5637-5646.
(24) Gond, R., Sada, K., Senthilkumar, B., and Barpanda, P. (2018) Bifunctional Electrocatalytic Behavior of Sodium Cobalt Phosphates in Alkaline Solution. *ChemElectroChem 5*, 153-158.

(25) Kanan, M. W., Yano, J., Surendranath, Y., Dincă, M., Yachandra, V. K., and Nocera, D. G. (2010) Structure and Valency of a Cobalt−Phosphate Water Oxidation Catalyst Determined by in Situ X-ray Spectroscopy. *Journal of the American Chemical Society 132*, 13692-13701.

(26) Kim, H., Park, J., Park, I., Jin, K., Jerng, S. E., Kim, S. H., Nam, K. T., and Kang, K. (2015) Coordination tuning of cobalt phosphates towards efficient water oxidation catalyst. *Nature Communications 6*.

(27) Lee, S. W., Carlton, C., Risch, M., Surendranath, Y., Chen, S., Furutsuki, S., Yamada, A., Nocera, D. G., and Shao-Horn, Y. (2012) The Nature of Lithium Battery Materials under Oxygen Evolution Reaction Conditions. *Journal of the American Chemical Society 134*, 16959-16962.

(28) Kim, T. K., Rustomii, C. S., Cho, H.-H., Chun, D., Jung, J.-Y., Caldwell, E., Kim, Y., Han, J. H., and Jin, S. (2016) Multi-wall carbon nanotube-embedded lithium cobalt phosphate composites with reduced resistance for high-voltage lithium-ion batteries. *Electron. Mater. Lett. 12*, 147-155.

(29) Hou, Y., Chang, K., Li, B., Tang, H., Wang, Z., Zou, J., Yuan, H., Lu, Z., and Chang, Z. (2018) Highly [010]-oriented self-assembled LiCOPO4/C nanoflakes as high-performance cathode for lithium ion batteries. *Nano Research 11*, 2424-2435.

(30) Hamers, R. J. (2017) Nanomaterials and Global Sustainability. *Accounts of Chemical Research 50*, 633-637.

(31) Kim, D.-H., and Kim, J. (2007) Synthesis of LiFePO4 nanoparticles and their electrochemical properties. *Journal of Physics and Chemistry of Solids 68*, 734-737.

(32) Ni, J. F., Zhou, H. H., Chen, J. T., and Zhang, X. X. (2005) LiFePO4 doped with ions prepared by co-precipitation method. *Materials Letters 59*, 2361-2365.

(33) Swierczynski, M., Stroe, D.-I., Stan, A.-I., Teodorescu, R., and Kaer, S. K. (2015) Lifetime Estimation of the Nanophosphate LiFePO4/C Battery Chemistry Used in. *IEEE Transactions on Industry Applications 51*, 3453-3461.

(34) Fergus, J. W. (2010) Recent developments in cathode materials for lithium ion batteries. *Journal of Power Sources 195*, 939-954.

(35) Cherkashinin, G., Lebedev, M. V., Sharath, S. U., Hajduk, A., Nappini, S., and Magnano, E. (2018) Exploring redox activity in a LiCoPO4–LiCo2P3O10 tailored positive electrode for 5 V lithium ion batteries: rigid band behavior of the electronic structure and stability of the delithiated phase. *Journal of Materials Chemistry A 6*, 4966-4970.

(36) Cherkashinin, G., Sharath, S. U., and Jaegermann, W. (2017) Toward Enhanced Electronic and Ionic Conductivity in Olivine LiCoPO4 Thin Film Electrode Material for 5 V Lithium Batteries: Effect of LiCo2P3O10 Impurity Phase. *Avanced Energy Materials 7*, 1602321.

(37) Ludwig, J., Geprägs, S., Nordlund, D., Doeff, M. M., and Nilges, T. (2017) Co11Li[(OH)5O][(PO3OH)(PO4)5], a Lithium-Stabilized, Mixed-Valent Cobalt(II,III) Hydroxide Phosphate Framework. *Inorganic Chemistry 56*, 10950-10961.

(38) Melby, E. S., Cui, Y., Borgatta, J., Hang, M. N., Gilder, J. M. V., Alvarez, C. M., Chrisler, W. B., Dohnalkova, A., Smith, J. N., Hamers, R. J., and Orr, G. Complex metal oxide and phosphate nanoparticles have fundamentally different impacts on rainbow trout gill epithelial cells. *Environ. Sci.: Nano (Submitted*.

(39) Borgatta, J., Ma, C., Hudson-Smith, N., Elmer, W., Pérez, C. D. P., Torre-Roche, R. D. L., Zuverza-Mena, N., Haynes, C., White, J. C., and Hamers, R. J. (2018) Copper Based

Nanomaterials Suppress Root Fungal Disease in Watermelon (C*itrullus lanatus)*: Role of Particle Morphology, Composition and Dissolution Behavior. *ACS Sustainable Chemistry and Engineering 6*, 14847–14856.

(40) Alarcón-Suesca, C., Ludwig, J., Hlukhyy, V., Stinner, C., and Nilges, T. (2016) In Situ Studies and Magnetic Properties of the *Cmcm* Polymorph of $LiCoPO_4$ with a Hierarchical Dumbbell-Like Morphology Synthesized by Easy Single-Step Polyol Synthesis. *Inorganics 4*, 35.

(41) Cohn, C. A., Pedigo, C. E., Hylton, S. N., Simon, S. R., and Schoonen, M. A. A. (2009) Evaluating the use of 3'-(*p*-Aminophenyl) fluorescein for determining the formation of highly reactive oxygen species in particle suspensions. *Geochemical Transactions 10*, 8.

(42) Cohn, C. A., Simon, S. R., and Schoonen, M. A. (2008) Comparison of fluorescence-based techniques for the quantification of particle-induced hydroxyl radicals. *Particle and Fibre Toxicology 5*.

(43) Kearns, D. B., and Losick, R. (2003) Swarming motility in undomesticated Bacillus subtilis. *Molecular Microbiology 49*, 581-590.

(44) Qiu, T. A., Nguyen, T. H. T., Hudson-Smith, N. V., Clement, P. L., Forester, D.-C., Frew, H., Hang, M. N., Murphy, C. J., Hamers, R. J., Feng, Z. V., and Haynes, C. L. (2017) Growth-Based Bacterial Viability Assay for Interference-Free and High-Throughput Toxicity Screening of Nanomaterials. *Analytical Chemistry 89*, 2057-2064.

(45) Feng, Z. V., Gunsolus, I. L., Qiu, T. A., Hurley, K. R., Nyberg, L. H., Frew, H., Johnson, K. P., Vartanian, A. M., Jacob, L. M., Lohse, S. E., Torelli, M. D., Hamers, R. J., Murphy, C. J., and Haynes, C. L. (2015) Impacts of gold nanoparticle charge and ligand type on surface binding and toxicity to Gram-negative and Gram-positive bacteria. *Chemical Science 6*, 5186-5196.

(46) Exnar, I., and Drezen, T. (2012) Synthesis of Nanoparticles of Lithium Metal Phosphate Positive Material for Lithium Secondary Battery, Dow Global Technologies LLC, US.

(47) Kreder, K. J., Assat, G., and Manthiram, A. (2015) Microwave-Assisted Solvothermal Synthesis of Three Polymorphs of LiCoPO ₄ and Their Electrochemical Properties. *Chemistry of Materials 27*, 5543-5549.

(48) Manzi, J., Curcio, M., and Brutti, S. (2015) Structural and Morphological Tuning of LiCoPO4 Materials Synthesized by Solvo-Thermal Methods for Li-Cell Applications. *Nanomaterials (Basel) 5*, 2212-2230.

(49) Sabnis, R. W. (2010) Newport Green DCF. *In Handbook of Biological Dyes and Stains: Synthesis an Industrial Applications*. John Wiley & Sons, Inc., Hoboken, NJ.

(50) Zhao, J., Bertoglio, B. A., Devinney Jr, M. J., Dineley, K. E., and Kar, A. R. (2009) The interaction of biological and noxious transition metals with zinc probes FluoZin-3 and Newport Green. *Anal Biochem. 384*, 34-41.

(51) Gunsolus, I. L., Hang, M. N., Hudson-Smith, N. V., Buchman, J. T., Bennett, J. W., Conroy, D., Mason, S. E., Hamers, R. J., and Haynes, C. L. (2017) Influence of nickel manganese cobalt oxide nanoparticle composition on toxicity toward Shewanella oneidensis MR-1: redesigning for reduced biological impact. *Environmental Science: Nano 4*, 636-646.

(52) Klein, N. D., Hurley, K. R., Feng, Z. V., and Haynes, C. L. (2015) Dark Field Transmission Electron Microscopy as a Tool for Identifying Inorganic Nanoparticles in Biological Matrices. *Analytical Chemistry 87*, 4356-4362.

(53) Anderson, R. C., Haverkamp, R. G., and Yu, P.-L. (2004) Investigation of morphological changes to Staphylococcus aureus induced by ovine-derived antimicrobial peptides using TEM and AFM. *FEMS Microbiology Letters 240*, 105-110.

(54) Hauser, H., and Shipley, G. G. (1984) Interactions of divalent cations with phosphatidylserine bilayer membranes. *Biochemistry 23*, 34-41.

(55) Mclaughlin, A. C. (1982) The Interaction of cobalt with glycerophosphoryl glycerol and phosphatidyl glycerol bilayer membranes. *Journal of Magnetic Resonance (1969) 49*, 246-256.

(56) Doğangün, M., Hang, M. N., Machesky, J., McGeachy, A. C., Dalchand, N., Hamers, R. J., and Geiger, F. M. (2017) Evidence for Considerable Metal Cation Concentrations from Lithium Intercalation Compounds in the Nano–Bio Interface Gap. *The Journal of Physical Chemistry C 121*, 27473-27482.

(57) Eitinger, T. (2013) Nickel, Cobalt Transport in Prokaryotes, In *Encyclopedia of Inorganic and Bioinorganic Chemistry* pp 1-10, John Wiley & Sons, Ltd, Chichester.

(58) Schauer, K., Rodionov, D. A., and de Reuse, H. (2008) New substrates for TonB-dependent transport: do we only see the 'tip of the iceberg'? *Trends in Biochemical Sciences 33*, 330-338.

(59) Ranquet, C., Ollagnier-de-Choudens, S., Loiseau, L., Barras, F., and Fontecave, M. (2007) Cobalt Stress in Escherichia coli. *Journal of Biological Chemistry 282*, 30442-30451.

(60) Thorgersen, M. P., and Downs, D. M. (2007) Cobalt targets multiple metabolic processes in Salmonella enterica. *Journal of Bacteriology 189*, 7774-7781.

(61) Barras, F., and Fontecave, M. (2011) Cobalt stress in Escherichia coli and Salmonella enterica: molecular bases for toxicity and resistance. *Metallomics 3*, 1130-1134.